Numerical study of turbulent flow over an S-shaped hydrofoil

T Micha Prem Kumar and Dhiman Chatterjee

Proceedings of the Institution of Mechanical Engineers, Part C: Journal of Mechanical Engineering Science 2008 222: 1717
DOI: 10.1243/09544062JMES929

Numerical study of turbulent flow over an S-shaped hydrofoil

T Micha Prem Kumar and **Dhiman Chatterjee***
Department of Mechanical Engineering, Indian Institute of Technology Madras, Chennai 600 036, India

The manuscript was received on 2 November 2007 and was accepted after revision for publication on 17 April 2008.

DOI: 10.1243/09544062JMES929

Abstract: In this paper, a numerical study of turbulent flow over the S-shaped hydrofoil at 0° angle of attack has been reported. Here, the flow takes place over concave and convex surfaces and is accompanied by the favourable and adverse pressure gradients and flow separation. Modelling such a flow poses a formidable challenge. In the present work four turbulence models, namely, k–ε realizable, k–ω shear stress transport, $\overline{v'^2}$–f, and the Reynolds stress model (RSM) were examined. Simulations were performed on a structured grid using finite-volume method formulation. Commercial software was used for grid generation and numerical simulation. A comparison of the experimental data of Madhusudan *et al.* (*Fluid Dyn. Res.*, 1994, **14**(5), 241–258) and numerical predictions were made, and the suitability of turbulence models was ascertained for both the mean and turbulent quantities. It was seen that $\overline{v'^2}$–f works better for predicting the mean quantities and the RSM for turbulent quantities.

Keywords: turbulent boundary layer, turbulence model, hydrofoil, pressure gradient effect, curvature effect, numerical simulation

1 INTRODUCTION

The turbulent flows that advance over the surface with curvature normal to the mean flow direction are common in many engineering applications. The effects of streamline curvatures on turbulent flows in many situations can be quite large [**1**].

In the past, the experimental studies of both internal flows within curved ducts and external flow around curved surfaces have been carried out [**2**–**5**]. From these careful experiments, it is evident that the turbulent shear stress is damped on convex surfaces [**2**], while the turbulent intensities inside the boundary layer increase in the presence of concave surfaces [**3**, **4**]. Baskaran *et al.* [**5**, **6**] studied the effect of the curvature and pressure gradient on the behaviour of turbulent flows. They showed that the shear stress is more sensitive to streamline curvature than the turbulent kinetic energy.

In the past, some efforts were made in solving the boundary-layer equations using different turbulent models. Gibson *et al.* [**7**] calculated the turbulent boundary layers on the curved surfaces by solving the boundary-layer equation with measured longitudinal pressure gradient, together with a Reynolds stress turbulence model and wall functions. In reality, the surface curvature effects are often accompanied by the pressure gradient effects and these need to be accounted for.

Richmond and Patel [**8**] carried out a numerical simulation of the flow inside a curved duct as well as an external flow over convex and concave surfaces. They used the k–ε model. Pressure distribution and velocity profile predictions matched well but the skin-friction coefficient and Reynolds stress data differed considerably from that of the experimental data.

Luo and Lakshminarayana [**9**, **10**] investigated the effects of strong convex and concave curvatures on the turbulent duct flow. They found that the Reynolds stress model (RSM) could successfully capture the damping of turbulence near the convex wall but underpredicted enhancement of turbulence near the concave wall. The difference in the relative success of the model to capture convex and concave curvatures may be attributed to the attenuation of existing eddies

*Corresponding author: Department of Mechanical Engineering, Indian Institute of Technology Madras, Chennai 600 036, India. email: dhiman@iitm@ac.in

by the convex structure and reorganization of eddy structures in the concave curvature.

Davidson [**11**] had predicted the flow around an aerofoil using the RSM. He concluded that in comparison with the two-layer k–ε model, the RSM could predict stall and flow features better. Rumsey and Gatski [**12**] studied the capabilities of three different turbulent models for predicting the effect of curvature on flow. They concluded that none of the one- or two-equation linear eddy viscosity models (EVM) and the algebraic stress model they had employed could fully capture the suppressed turbulence near the convex wall or the enhanced turbulence near the concave wall. The RSM could capture the suppression of turbulence. Sleiti and Kapat [**13**] compared the performance of two-equation eddy viscosity and RSM for simulating flow and heat transfer in rotating rib-roughened internal cooling channels. They concluded that overall the RSM performed better than the EVM. Jing-lei *et al.* [**14**] used linear and non-linear EVM, a quadratic algebraic stress model, and the RSM for predicting flows having strong curvature effects. Yakinthos *et al.* [**15**] simulated flow in a 90° rectangular duct by applying three low-Reynolds-number turbulence models – two EVMs and a RSM. In general, the RSM was seen to give results consistent with the experimental values, but its predictive capability was poor near the concave wall. From the above studies, it is clear that the effects of curvature on the velocity profiles and turbulence intensity must be predicted accurately to capture the boundary layer development over the curved surface.

In contrast to the conventional symmetric or single cambered aerofoil, attention is given here to the flow over a double-cambered S-shaped hydrofoil. This type of aerofoil profile is used in runner blades of the fully reversible pump-turbine that finds application in tidal power plants and thermal power plants for providing peaking power [**16**].

An S-blade profile has consecutive concave and convex curvatures on both the upper and lower surfaces (Fig. 1). The boundary layers develop under the simultaneous effect of the concave and convex curvatures and favourable and adverse pressure gradients. Further, the boundary layer over the upper surface encounters the convex surface first and then the concave surface, whereas the flow over the lower surface experiences the reverse order of curvatures.

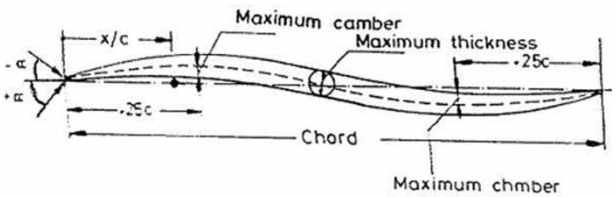

Fig. 1 Geometry of S-blade (S3525)

These blades are represented by a four-digit number preceded by S [**16**]. The first and second digits represent the maximum camber and maximum thickness, respectively, as percentage of chord, and the last two digits together give the location of maximum camber as percentage of chord from either end. In the present work, the S3525 profile, which may be better suited as a runner blade in a reversible pump-turbine [**17**], has been used.

An accurate prediction of the flow past an S-blade will depend on the choice of the turbulence model. It is a known fact that there is no single turbulence model that can be applied for all flow situations. So, it becomes necessary to examine the predictive capabilities of some of the possible turbulence models against the experimental data available.

Strictly speaking, the only fundamentally secure approach to simulate turbulent flow is to use direct numerical simulation (DNS) that can resolve the entire turbulent spectrum. Alternatively, large eddy simulations (LES) may be employed, in which the smaller eddies are filtered and are modelled using a subgrid scale model, whereas the larger energy carrying eddies are simulated. Naturally, DNS requires larger computational resources than the LES. However, for most practical problems, not only the DNS but also the LES poses a prohibitively large computational resource because near a wall, large dynamically influential turbulent scales are small, and so a very dense mesh is required [**18**]. For most practical problems, therefore, Reynolds-averaged Navier–Stokes (RANS) equations are employed with appropriate closure models to simulate the flow.

There are two broad classifications of RANS, namely, EVM and RSM. Two of the most well-known and popular RANS models are k–ε and k–ω, and their variants [**19**]. Durbin [**20**] successfully used the k–ε–$\overline{v'^2}$ model for the turbulent separated flows over a backward facing step, in a plane diffuser and also around a triangular cylinder. Good agreement with the experimental result was found, in this case, of massive separation and smooth separation. Iaccarino [**21**] carried out the computation of turbulent flow in an asymmetric two-dimensional diffuser and reported that the result obtained using the $\overline{v'^2}$–f model was consistent with the experimental data.

In this study, a numerical simulation of a two-dimensional turbulent flow over an S-blade for four different turbulence models has been carried out. These models are k–ε realizable, $\overline{v'^2}$–f, k–ω shear stress transport (SST), and the RSM. From the survey of literature on turbulence modelling available, it is clear that the EVMs find application in a wide range of practical problems and the RSM is particularly useful in predicting flows, where anisotropy could be significant. This has also led to the inclusion of these models

in commercial computational fluid dynamics (CFD) software.

The main objective of the work is to compare the predictive capabilities of these models for the simulation of turbulent flow over surfaces having consecutive concave and convex curvatures. The numerical methods and turbulence models with the appropriate equations are presented in section 2. Simulation procedure including grid generation is also covered in section 2, results and discussions are given in section 3, and conclusion in section 4.

2 GOVERNING EQUATIONS AND NUMERICAL SCHEME

The governing equations for steady, incompressible fluid are

$$\frac{\partial u_i}{\partial x_i} = 0 \tag{1}$$

$$u_i \frac{\partial u_j}{\partial x_i} = \frac{\partial}{\partial x_j}\left[(\nu + \nu_t)\frac{\partial u_i}{\partial x_j}\right] - \frac{1}{\rho}\frac{\partial p}{\partial x_j} \tag{2}$$

Instantaneous Navier–Stokes equations can be time averaged, in order to transform it into the RANS equation in such a way that the small-scale turbulent fluctuations do not have to be simulated directly. This transformation introduces an additional Reynolds stresses $-\rho\overline{u_i' u_j'}$ term in the governing equation that needs to be modelled in order to achieve 'closure'. This is achieved through the different turbulence models. The next section is an introduction about the different turbulent models used in this work.

2.1 Turbulence modelling

Different turbulent models are available and, based on the existing knowledge of 'success' and 'failure' of these models in solving the different flow situations, four models have been identified for the present work, which involves the flow where streamline curvature, pressure gradient effects can be significant and where flow separation is expected. In the order of increasing complexity, these are k–ε realizable, k–ω SST, $\overline{v'^2}$–f, and the RSM. These models are briefly described in the next subsection. The first three models are the EVM, whereas the last one is a second moment closure model.

2.1.1 k–ε realizable model

The modelled transport equations for k and ε in the k–ε realizable model are [**22**]

$$\frac{\partial}{\partial x_j}(ku_j) = \frac{\partial}{\partial x_j}\left[\left(\nu + \frac{\nu_t}{\sigma_k}\right)\frac{\partial k}{\partial x_j}\right] + P - \varepsilon \tag{3}$$

and

$$\frac{\partial}{\partial x_j}(\varepsilon u_j) = \frac{\partial}{\partial x_j}\left[\left(\nu + \frac{\nu_t}{\sigma_\varepsilon}\right)\frac{\partial \varepsilon}{\partial x_j}\right] + C_1 S\varepsilon - C_2\frac{\varepsilon^2}{k + (\nu\varepsilon)^{1/2}} \tag{4}$$

where

$$C_1 = \max\left[0.43, \frac{\eta}{\eta + 5}\right] \tag{5}$$

$$\eta = S\frac{k}{\varepsilon} \tag{6}$$

$$S = \left(2S_{ij}S_{ij}\right)^{1/2} \tag{7}$$

In these equations, P represents the generation of turbulence kinetic energy due to the mean velocity gradients, σ_k and σ_ε are the turbulent Prandtl numbers for k and ε, respectively. In the present work, the model constants being used are $C_2 = 1.9, \sigma_k = 1$, and $\sigma_\varepsilon = 1.2$.

In order to best account for surface roughness, semi-empirical equations in the form of an 'enhanced wall treatment' with 'pressure gradient effect' are used to bridge the viscosity-affected region between the wall and the fully turbulent region. The two-layer approach is an integral part of the enhanced wall treatment and is used to specify both ε and the turbulent viscosity in the near-wall cell. In this approach, the whole domain is subdivided into a viscosity-affected region and a fully turbulent region. The demarcation of the two regions is determined by a wall-distance-based turbulent Reynolds number

$$Re_y = \frac{\rho y\sqrt{k}}{\mu} \tag{8}$$

where y is the normal distance from the wall at the cell centres.

In the fully turbulent region ($Re_y > Re_y^+; Re_y^+ = 200$), standard k–ε model is employed.

In the viscosity-affected near-wall region, ($Re_y < Re_y^+$)μ_t is computed from

$$\mu_{t,2layer} = \rho C_\mu l_\mu \sqrt{k} \tag{9}$$

where l_μ is calculated from

$$l_\mu = yC_l\left(1 - e^{-R_{ey}/A_\mu}\right) \tag{10}$$

The two-layer formulation for turbulent viscosity described above is used as a part of the enhanced wall treatment, in which the two-layer definition is smoothly blended with the high-Reynolds number μ_t definition from the outer region

$$\mu_{t,enh} = \lambda_\varepsilon \mu_t + (1 - \lambda_\varepsilon)\mu_{t,2layer} \tag{11}$$

where μ_t is the high-Reynolds number definition as described for the standard k–ε model.

A blending function λ_ε is defined in such a way that it is equal to unity far from the walls and is zero very near to the walls. The blending function chosen is

$$\lambda_\varepsilon = \frac{1}{2}\left[1 + \tanh\left(\frac{Re_y - Re_y^+}{A}\right)\right] \tag{12}$$

The constant A determines the width of the blending function. It is defined such that the value of λ_ε will be within 1 per cent of its far-field value, given a variation of ΔRe_y.

The ε field is computed from

$$\varepsilon = \frac{k^{3/2}}{l_\varepsilon} \tag{13}$$

The length scale $l_\varepsilon = yC_l\left(1 - \mathrm{e}^{-Re_y/A_\varepsilon}\right)$.

The constants in the length scale formula are

$$C_\mathrm{l} = kC_\mu^{-3/4}, \quad A_\mu = 70, \quad A_\varepsilon = 2C_\mathrm{l}$$

2.1.2 $\overline{v'^2}$–f model

The $\overline{v'^2}$–f turbulence model is an alternative to the k–ε model and was introduced to model the near-wall turbulence without the use of exponential damping or wall functions [**21**]. The turbulence model described earlier uses turbulence kinetic energy, k, as the velocity scale in the eddy viscosity region. However, it is well known that the turbulence is anisotropic near the wall, and so k is not a good representative of the velocity scale. Shear stress is driven by the normal stress, $\overline{v'^2}$, in the near-wall layer. In the enhanced model formulation described earlier, a damping function is used to account for more rapid decay in wall-normal intensity than that of the turbulent energy. This damping is assumed to be purely viscous and in reality, viscous damping occurs over a thinner region than is implied in the damping function [**18**]. To overcome these difficulties, the $\overline{v'^2}$–f model was developed by Durbin [**20**]. It incorporates a simplified transport equation for the normal stress perpendicular to the streamlines (or, the wall) that serve as the turbulent-velocity scale in the eddy viscosity, in preference to the turbulence energy. The model requires the solution of four differential equations

$$u_i\frac{\partial k}{\partial x_i} = P - \varepsilon + \frac{\partial}{\partial x_j}\left[\left(\nu + \frac{\nu_t}{\sigma_k}\right)\frac{\partial k}{\partial x_j}\right] \tag{14}$$

$$u_i\frac{\partial \varepsilon}{\partial x_i} = \frac{f_1 C_{\varepsilon 1}P - f_2 C_{\varepsilon 2}\varepsilon}{T} + \frac{\partial}{\partial x_j}\left[\left(\nu + \frac{\nu_t}{\sigma_\varepsilon}\right)\frac{\partial \varepsilon}{\partial x_j}\right] \tag{15}$$

The eddy viscosity is obtained from

$$\nu_\mathrm{t} = C_\mu f_\mu kT \tag{16}$$

where

$$f_1 = 1 + 0.045\left(\frac{k}{\overline{v'^2}}\right)^{1/2} \tag{17}$$

$$f_2 = 1 \tag{18}$$

$$f_\mu = \frac{\overline{v'^2}}{k} \tag{19}$$

$$T = \max\left[\frac{k}{\varepsilon}, 6\left(\frac{\nu}{\varepsilon}\right)^{1/2}\right] \tag{20}$$

The equations model the turbulence velocity scale $\overline{v'^2}$ and its production, kf

$$u_i\frac{\partial \overline{v'^2}}{\partial x_i} = kf - 6\overline{v'^2}\frac{\varepsilon}{k} + \frac{\partial}{\partial x_j}\left[\left(\nu + \frac{\nu_\mathrm{t}}{\sigma_k}\right)\frac{\partial \overline{v'^2}}{\partial x_j}\right] \tag{21}$$

$$f - L^2\frac{\partial^2 f}{\partial x_j \partial x_j} = C_1\frac{\left(2/3 - \overline{v'^2}/k\right)}{T} + C_2\frac{P}{k} + \frac{5\overline{v'^2}/k}{T} \tag{22}$$

where L is the length scale and is defined as

$$L^2 = C_\mathrm{l}^2 \max\left[\frac{k^3}{\varepsilon^2}, C_\eta^2\left(\frac{\nu^3}{\varepsilon}\right)^{1/2}\right] \tag{23}$$

The constants used in the present simulations are as follows $C_{\varepsilon 1} = 1.4$, $C_{\varepsilon 2} = 1.9$, $C_\mu = 0.22$, $C_\mathrm{l} = 0.23$, $C_\eta = 70$, $C_1 = 1.4$, $C_2 = 0.3$, $\sigma_k = 1$, and $\sigma_\varepsilon = 1.3$.

The eddy-viscosity damping is provided in this case by the presence of $\overline{v'^2}$ (equation (19)). In other words, the amount of damping is controlled by the ratio of $\overline{v'^2}$ and k instead of the turbulent Reynolds number Re_t, like in the k–ε model.

2.1.3 k–ω SST (the shear-stress transport model)

k–ω model performs better than the k–ε model near the wall. However, there is one problem with k–ω model – its extreme sensitivity to the value of ω at irrotational boundaries of shear flows. This led Menter [**23**] to formulate a hybrid model, which blends the advantages of k–ω model near the wall (typically, $y^+ < 70$) and k–ε model away from the wall. This model, SST model, performs satisfactorily in the decelerating boundary layer and is thus effective in predicting separation. The transport equations for the k–ω SST model are as given below [**22**]

$$\frac{\partial}{\partial x_j}(ku_i) = \frac{\partial}{\partial x_j}\left(\frac{\Gamma_k}{\rho}\frac{\partial k}{\partial x_j}\right) + P + Y_k \tag{24}$$

$$\frac{\partial}{\partial x_j}(\omega u_i) = \frac{\partial}{\partial x_j}\left(\frac{\Gamma_\omega}{\rho}\frac{\partial \omega}{\partial x_j}\right) + G_\omega - Y_k + D_\omega \tag{25}$$

In these equations, P represents the generation of turbulent kinetic energy due to mean velocity gradients and G_ω represents the generation of ω. Γ_k and Γ_ω represent the effective diffusivity of k and ω,

respectively. Y_k and Y_ω represent the dissipation of k and ω, respectively, due to turbulence. D_ω represents the cross-diffusion term.

For all the EVM discussed above, the turbulent stresses $\bar{u}'^2$, $\bar{v}'^2$, and $-\overline{u'v'}$ are calculated based on the Boussinesq assumption.

2.1.4 *Reynolds stress model (RSM)*

Most models used in engineering practice employ the Boussinesq approximation, where the turbulent stresses in the Reynolds-averaged momentum and energy equations are assumed equal to the product of the isotropic eddy viscosity coefficient and mean velocity strain rate. However, when the Boussinesq assumption is not valid, Reynolds stress calculations will be in error regardless of how accurately the model equations are solved. The RSM, which does not use the Boussinesq assumption, is considered to be of a higher level of closure that is available. These models are superior to the algebraic, one- and two-equation models since they eliminate the assumption that the turbulent stresses and respond to changes in the mean strain rate. They also account for anisotropy of turbulence and extra effects (e.g. streamline curvature and rotation). However, many unknown turbulent quantities are required for the RSM and these are usually obtained by assuming that the turbulence is locally homogeneous and in equilibrium. These models are currently too CPU-intensive for most engineering calculations, and have yet to be applied to many complex flows, particularly wall-bounded flows. In addition, numerical stability problems may arise due to the absence of turbulent viscosity, making the application in complicated situations difficult at present. In the RSM, the Boussinesq assumption is not used but a partial differential equation (transport equation) for the stress tensor is derived from the Navier–Stokes equation. The exact transport equations for the transport of the Reynolds stresses, $\rho\overline{u_i'u_j'}$, may be written as follows [**22**]

$$\underbrace{\frac{\partial}{\partial x_k}\left(\rho u_k \overline{u_i'u_j'}\right)}_{\text{Convection } C_{ij}} = \underbrace{\frac{\partial}{\partial x_k}\left[\rho\overline{u_i'u_j'u_k'} + \overline{p\left(\delta_{kj}u_i' + \delta_{ik}u_j'\right)}\right]}_{\text{Turbulent diffusion } D_{\mathrm{T},ij}} + \underbrace{\frac{\partial}{\partial x_k}\left(\mu\frac{\partial}{\partial x_k}\overline{\left(u_i'u_j'\right)}\right)}_{\text{Molecular diffusion } D_{\mathrm{L},ij}} - \underbrace{\rho\left(\overline{u_i'u_k'}\frac{\partial u_j}{\partial x_k} + \overline{u_j'u_k'}\frac{\partial u_i}{\partial x_k}\right)}_{\text{Stress production } P_{ij}} + \underbrace{\overline{p\left(\frac{\partial u_i'}{\partial x_j} + \frac{\partial u_j'}{\partial x_i}\right)}}_{\text{Pressure strain } \phi_{ij}} - \underbrace{2\mu\overline{\left(\frac{\partial u_i'}{\partial x_k}\frac{\partial u_j'}{\partial x_k}\right)}}_{\text{Dissipation } \varepsilon_{ij}} \tag{26}$$

Some terms are unknown in equation (26), such as: the turbulent diffusion term, pressure–strain, and dissipation tensor. From the Navier–Stokes equation, transport equations can be derived for these unknown quantities but this would add further unknowns to the equation system. Instead these terms need to be modelled to close the equation.

Modelling turbulent diffusive transport

$$D_{\mathrm{T},ij} = \frac{\partial}{\partial x_k}\left(\frac{\mu_\mathrm{t}}{\sigma_k}\frac{\partial u_i'\partial v_j'}{\partial x_k}\right) \tag{27}$$

The turbulent viscosity, μ_t, is computed in a way similar to that of k–ε model and $\sigma_k = 0.82$.

Modelling the pressure–strain term

The pressure–strain term contains: $\phi_{ij,1}$, the slow pressure–strain term, also known as the return-to-isotropy term; $\phi_{ij,2}$, the rapid pressure–strain; and $\phi_{ij,\mathrm{w}}$, the wall-reflection term

$$\phi_{ij} = \phi_{ij,1} + \phi_{ij,2} + \phi_{ij,\mathrm{w}} \tag{28}$$

The slow pressure–strain term, $\phi_{ij,1}$, is modelled as

$$\phi_{ij,1} = -C_1\rho\frac{\varepsilon}{k}\left(\overline{u_i'v'}_i - \frac{2}{3}\delta_{ij}k\right) \tag{29}$$

$$C_1 = 1.8$$

The rapid pressure–strain term, $\phi_{ij,2}$, is modelled as

$$\phi_{ij,2} = -C_2\left[\left(P_{ij} - C_{ij}\right) - \frac{2}{3}\delta_{ij}\left(P - C\right)\right] \tag{30}$$

$$C_2 = 0.6$$

P_{ij} and C_{ij} are defined as in equation (26)

$$P = \frac{1}{2}P_{kk}, \quad C = \frac{1}{2}C_{kk}$$

The wall-reflection term, $\phi_{ij,\mathrm{w}}$, is responsible for the redistribution of normal stresses near the wall. It tends to damp the normal stress perpendicular to the wall, while enhancing the stresses parallel to the wall. This term is modelled as

$$\phi_{ij,w} = C_1'\frac{\varepsilon}{k}\left(\overline{u_k'u_m'}n_kn_m\delta_{ij} - \frac{3}{2}u_i'u_k'n_jn_k - \frac{3}{2}u_j'u_k'n_in_k\right)\frac{k^{3/2}}{C_l\varepsilon d} + C_2'\left(\phi_{km,2}n_kn_m\delta_{ij} - \frac{3}{2}\phi_{ik,2}n_jn_k - \frac{3}{2}\phi_{jk,2}n_in_k\right)\frac{k^{3/2}}{C_l\varepsilon d} \tag{31}$$

where $C_1' = 0.6$, $C_2' = 0.5$, n_k is the x_k component of the unit normal to the wall, d is the normal distance to the wall, and $C_l = C_\mu^{3/4}/\kappa$, where $C_\mu = 0.09$ and κ is the von Karman constant (= 0.4187).

The dissipation tensor, ε_{ij}, is modelled as

$$\varepsilon_{ij} = \frac{2}{3}\delta_{ij}\rho\varepsilon \tag{32}$$

The scalar dissipation rate ε is computed with a model transport equation similar to that used in the k–ε model.

2.2 Numerical scheme

A finite-volume code (Fluent®) solves the discretized equations in a segregated manner, with the SIMPLEC (semi-implicit method for pressure-linked equation-consistent) algorithm. In the SIMPLEC algorithm, the continuity equation (equation (1)) is converted into a discrete Poisson equation for pressure. The differential equations are linearized and solved implicitly in sequence: starting with the pressure equation (predictor stage), followed by the momentum equations and pressure correction equation (corrector stage). The equations for the scalars (turbulent quantities) are solved after updating both the pressure and velocity components. In Table 1, a summary of the numerical parameters used for the computations are reported.

2.3 Statement of the problem

A two-dimensional computational domain is used in the present case. The chord length of the hydrofoil is 0.3 m. The inlet boundary condition is kept at a distance 10 times the chord length upstream of the leading edge of the hydrofoil. The height of the domain above and below the profile is six times the chord length. The outlet boundary condition is kept at a distance 20 times the chord length of the trailing edge of the hydrofoil. Simulation of flow in the domain was carried out subjected to the boundary conditions described below, and both the mean and turbulent quantities were predicted. The numerical predictions were then compared with the experimental data available [**24**].

2.3.1 *Boundary condition*

Uniform flow velocity of 22.5 m/s was imposed at the velocity inlet and atmospheric pressure was prescribed at the pressure outlet condition of the domain. No-slip boundary conditions were set on the hydrofoil surface and wall. The values of turbulence intensity and length scale were obtained from the relations $0.13 \times Re^{(-1/8)}$ and $0.07 \times D_h$, respectively, where D_h is the hydraulic diameter and Re is the Reynolds number based on the chord length and velocity at the inlet, and its value is 4.5×10^5. Air was used as the working medium for simulation. All the simulations were done at 0° angle of attack.

2.3.2 *Grid sensitivity test*

Grid generation requires careful consideration in the selection of mesh size, spacing, and the number of grids. In the present work, the grid dependency test was carried out to arrive at the optimum grid counts. Five different grids have been tested with 56 594, 136 363, 265 164, 402 124, and 586 304 nodes. The grid was refined and tests continued until the grid independent solution of drag (C_D) and lift (C_L) coefficients were obtained as shown in Fig. 2. The optimum grids of 402 124 nodes have been chosen based on C_D and C_L as shown in Fig. 2. Strong clustering of the grid points at the profile has been used, so that the y^+ of the grid points away from the foil surface was <1.

3 RESULTS AND DISCUSSION

3.1 Aerodynamic performance

In Table 2, a summary of C_L, C_D, and C_L/C_D values at 0° angle of attack for these different models are given. Negative values of C_L and C_L/C_D are the important characteristics for the pump to operate in the reverse direction. These values match with the experimental results of Madhusudan [**25**], and both $\overline{v'^2}$–f and the RSM yield results closest to the experimental data.

Table 1 Numerical parameters used for the simulations

	Spatial discretization			Pressure correction	Under-relaxation							
							TQ					
	U, V	P	TQ		U, V	P	TKE	TDR	TV	RS	VVS	ERF
k–ε realizable	FOU	Linear	FOU	SIMPLEC	0.7	0.3	0.8	0.8	1	—	—	—
k–ω SST	SOU	Linear	SOU	SIMPLEC	0.4	0.25	0.58	0.52	0.94	—	—	—
$\overline{v'^2}$–f	FOU	Standard	FOU	SIMPLE	0.7	0.3	0.8	0.8	1	—	0.6	0.6
RSM	FOU	Standard	FOU	SIMPLEC	0.3	0.25	0.5	0.7	0.9	0.4	—	—

U, V, mean velocity components; P, pressure; TQ, turbulent quantities; FOU, first-order upwind; SOU, second-order upwind; TKE, turbulent kinetic energy; TDR, turbulent dissipation rate; TV, turbulent viscosity; RS, Reynolds stress; VVS, velocity variance scale; ERF, elliptic relaxation function.

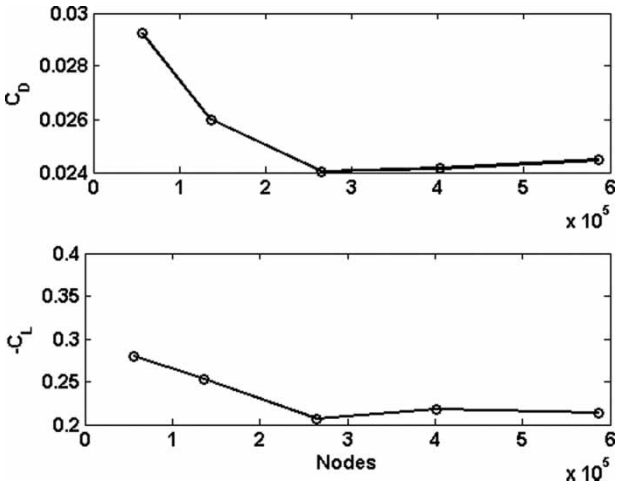

Fig. 2 Determination of number of grids required to arrive at grid independent solution

Table 2 Summary of aerodynamic characteristics at 0° angle of attack

	C_L	C_D	C_L/C_D
Experimental [**25**]	−0.207	0.0181	−11.4
$k-\varepsilon$ realizable	−0.217	0.0241	−9.0
$k-\omega$ SST	−0.151	0.0199	−7.6
$\overline{v'^2}-f$	−0.214	0.0221	−9.7
RSM	−0.209	0.0229	−9.1

3.2 Prediction of mean quantities

Figure 3 shows the pressure distribution on the S-shaped hydrofoil. Experimental data [**24**] are compared with the four turbulence models. These results indicate that on both the surfaces all models predict equally well.

Figure 4(a) shows the variation of the skin-friction co-efficient (C_f) on the lower surface. Streamwise distance is normalized with the chord length. A comparison is made with the skin-friction coefficient obtained from the different models and the experimental data of Madhusudan *et al.* [**24**]. The experiment shows reattachment at $x/c = 0.20$. The $\overline{v'^2}-f$ model predicts at 0.16, the $k-\omega$ SST model predicts at $x/c = 0.14$, the $k-\varepsilon$ realizable model predicts at $x/c = 0.11$, and the RSM predicts at $x/c = 0.10$. In the region between $x/c = 0.2$ and $x/c = 0.5$, C_f increases as pressure decreases, whereas the concave curvature should have reduced C_f. This shows that the curvature effect is less significant. This is borne by the fact that the maximum value of (δ/R) is about 0.002. Between $x/c = 0.5$ and $x/c = 0.8$, the adverse pressure gradient and convex curvature effects work together to bring a reduction of C_f. Beyond $x/c = 0.8$, though the pressure gradient is again favourable, yet the value of C_f is decreasing, indicating the curvature effect to be strong. It may be mentioned that in this region the curvature effect, signified by the ratio of (δ/R), is about 0.5, indicating a very strong curvature effect. All the turbulent models capture the curvature and pressure gradient effects properly.

Figure 4(b) shows the variation of C_f on the upper surface. It is well known that for the flow over a flat plate under the influence of favourable pressure gradient, C_f value should increase. However, in the present case, the value of C_f decreases along the streamwise direction as shown in Fig. 4(b). This indicates that the effect of curvature is predominant compared with the effect of pressure gradient in the region. Numerically, all the models predict the rise and fall in the C_f value as shown in experimental results. However, none of these models could predict the small separation zone (between $x/c = 0.4$ and 0.5) that was seen in the experiment.

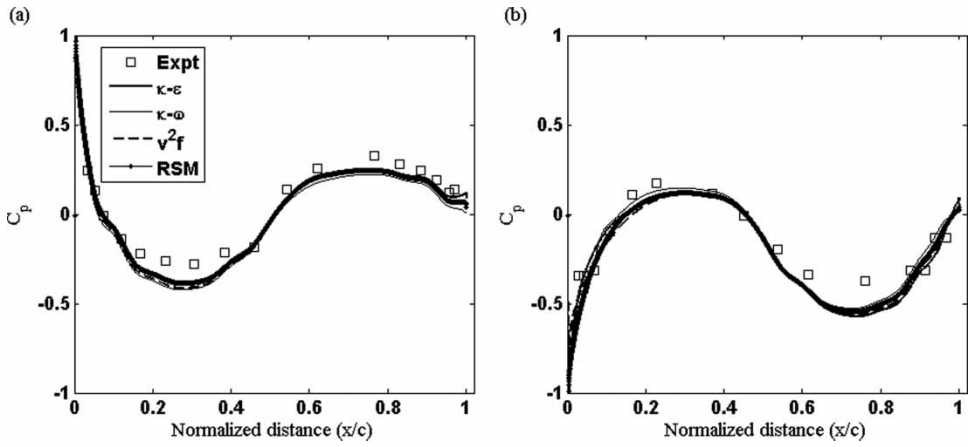

Fig. 3 Variation of coefficient of pressure along (a) upper and (b) lower surfaces. Expt: experimental data [**24**]; $k-\varepsilon$: $k-\varepsilon$ realizable; $k-\omega$: $k-\omega$ SST; v^2f: $\overline{v'^2}-f$; RSM: Reynolds stress model

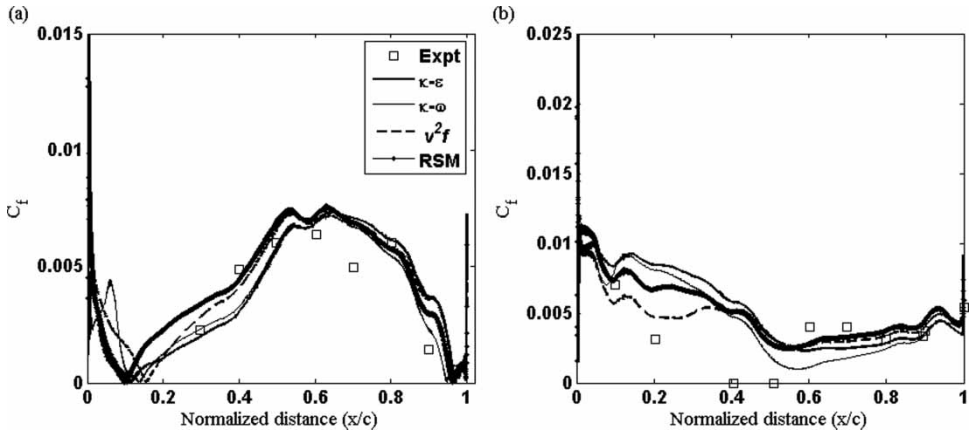

Fig. 4 Variation of skin-friction coefficient along (a) lower and (b) upper surfaces. Expt: experimental data [**24**]; k–ε: k–ε realizable; k–ω: k–ω SST; v^2f: $\overline{v'^2}$–f; RSM: Reynolds stress model

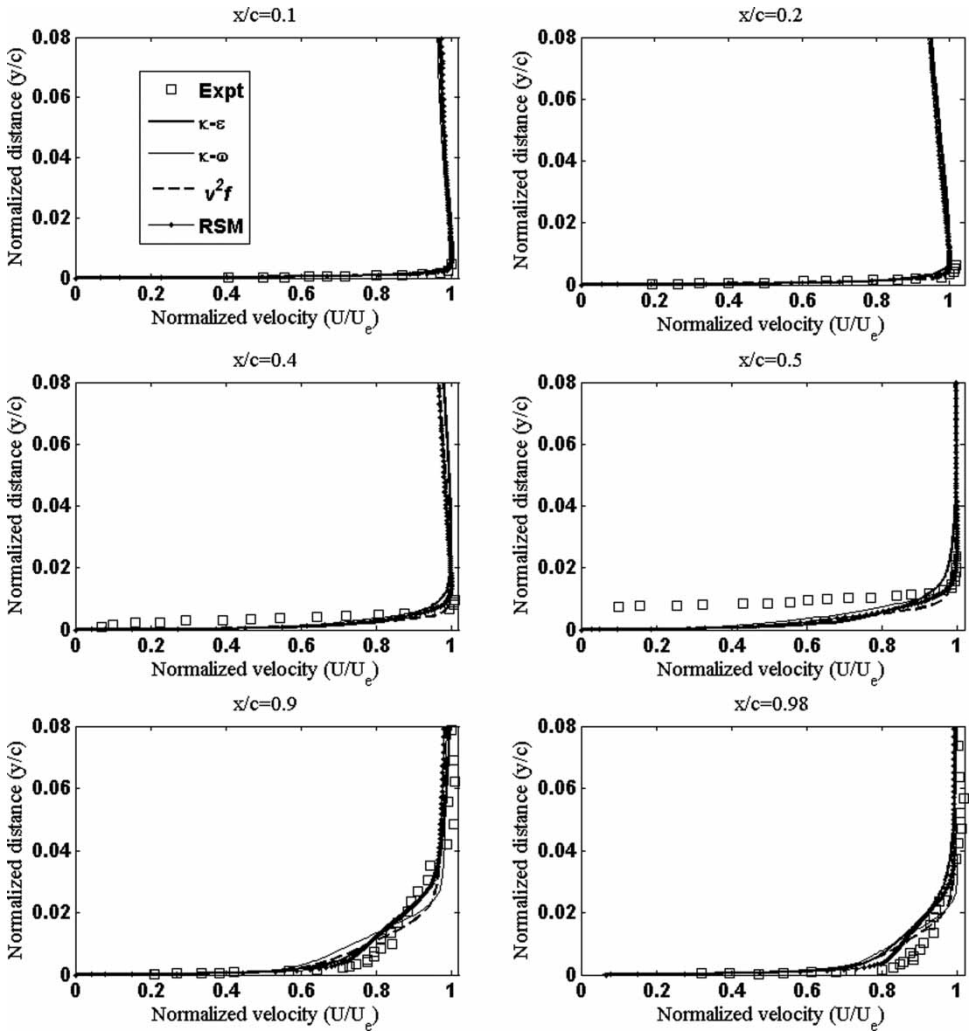

Fig. 5 Velocity distributions across the boundary layer on the upper surface of the hydrofoil. Expt: experimental data [**24**]; k–ε: k–ε realizable; k–ω: k–ω SST; v^2f: $\overline{v'^2}$–f; RSM: Reynolds stress model

3.2.1 *Upper surface*

The velocity distributions on the upper surface of the S-shaped hydrofoil at different locations are reported in Fig. 5. The profiles are taken normal to the hydrofoil surface. It may be noted that the local velocity at the edge of the boundary layer is used to normalize the experimentally obtained and numerically predicted velocities. It is seen that all the models capture the experimental trend quite well except at $x/c = 0.5$, where a small separation was observed experimentally. From the numerically

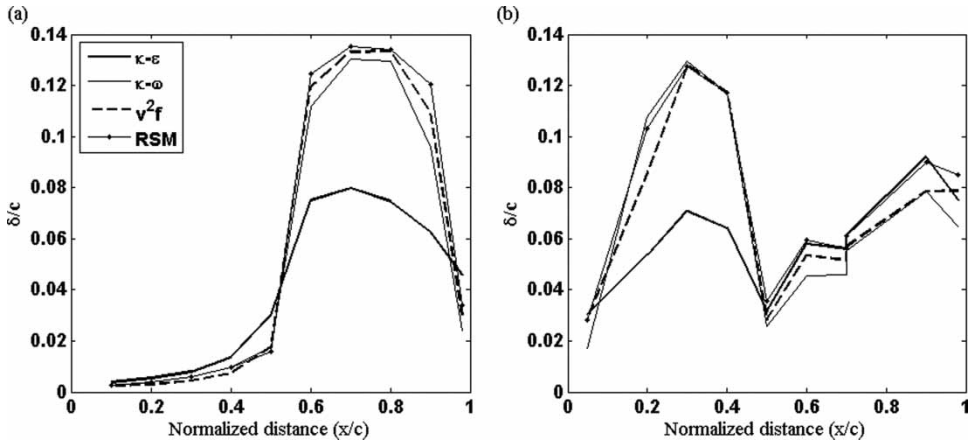

Fig. 6 Variation of boundary-layer thickness along (a) upper and (b) lower surfaces. k–ε: k–ε realizable; k–ω: k–ω SST; v^2f : $\overline{v'^2}$–f; RSM: Reynolds stress model

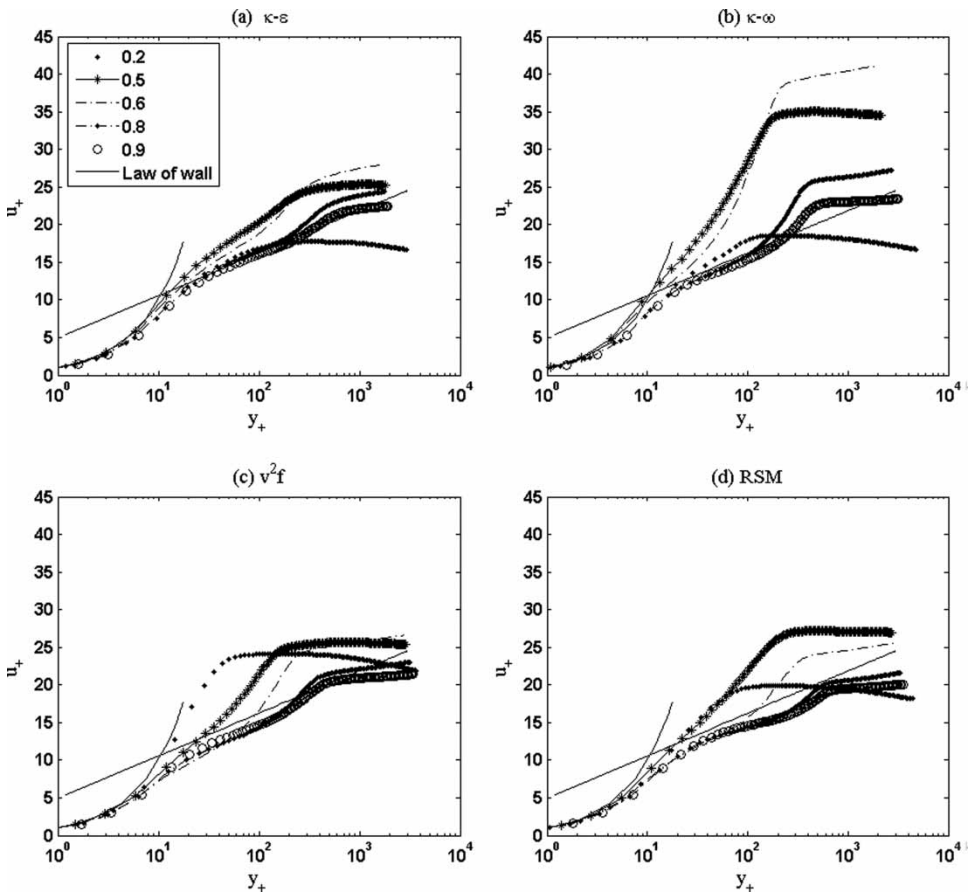

Fig. 7 Semi-logarithmic plots of velocity profiles at different stations on the upper surface. k–ε: k–ε realizable; k–ω: k–ω SST; v^2f: $\overline{v'^2}$–f; RSM: Reynolds stress model

predicted velocity profiles, the boundary-layer thickness was determined at different locations on upper and lower surfaces. These are shown in Fig. 6.

Figure 7 shows the non-dimensional velocity distributions at stations $x/c = 0.2$, 0.5, 0.6, 0.8, and 0.9 in the boundary layer for the different turbulence models. It can be noticed that in the viscous sublayer (about $y^+ \leqslant 5$) all the curves coincide with each other irrespective of their locations, as is the case with the boundary layer over a flat plate. However, in the overlap region, there is a big difference due to curvature in the S-shaped profile. From Fig. 6(a), it can be seen that there is an increase in the boundary-layer thickness in the upper surface till $x/c = 0.8$. Correspondingly, there is a decrease in the slope of the log–law region predicted by the RSM and $\overline{v'^2}$–f models. This feature was also reported by Lueptow *et al.* [**26**]. At the trailing edge, there is an increase in the slope of the log–law region due to a decrease in the boundary-layer thickness.

3.2.2 *Lower surface*

The velocity distributions in the boundary layer for the different models on the lower surface of the hydrofoil are reported in Fig. 8. Here also, the local velocity at the edge of the boundary layer was used to normalize the velocities. It was seen that, except at $x/c = 0.2$, the velocities have been predicted well by all the models with $\overline{v'^2}$–f and the RSM being the closest to the experimental values. As mentioned before, all the models had underpredicted the separation region and this is clear from the velocity profiles at $x/c = 0.2$. Careful observation of this figure and the corresponding figure for the upper surface (Fig. 5) suggests that the models cannot capture the effects of change of the curvature

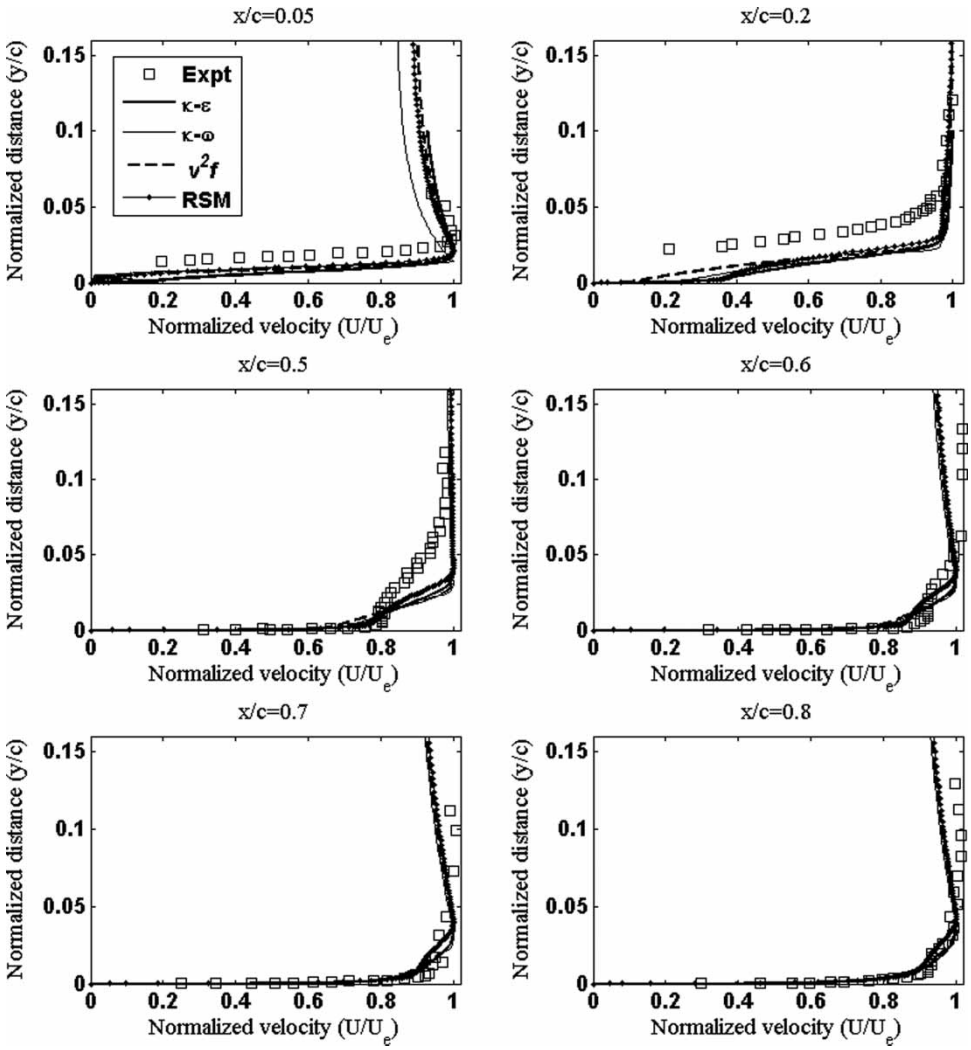

Fig. 8 Velocity distributions across the boundary layer on the lower surface of the hydrofoil. Expt: experimental data [**24**]; k–ε: k–ε realizable; k–ω: k–ω SST; v^2f: $\overline{v'^2}$–f; RSM: Reynolds stress model

(from convex to concave on the upper surface and reverse on the lower one) very accurately.

Figure 9 shows the semi-logarithmic plot of velocity profile at different stations on the lower surface. In the viscous sublayer, there is not much difference between the flat plate boundary layer and S-shaped profile at different locations. This was also observed by Willmarth *et al.* [**27**] and Lueptow *et al.* [**26**]. However, in the overlap region and outer turbulent layer, there is a significant deviation from the logarithmic trend of flat plate boundary layer. At $x/c = 0.2$ and 0.9, the slope of log-law region is more than the corresponding region for a flat plate. The boundary-layer thickness increases, as shown in Fig. 6(b), till $x/c = 0.3$ and the slope of the log–law region decreases, similar to the observation of Lueptow *et al.* [**26**]. Beyond $x/c = 0.5$, the boundary-layer thickness increases but the slope of the log–law region increases. This is due to the significant curvature effect on this portion of the lower surface. It may be pointed out in this context that the curvature effect is more significant in the region $x/c > 0.5$, whereas in the region $x/c < 0.5$, the curvature is insignificant and the results confirm the role played by the curvatures.

3.3 Prediction of fluctuating quantities

3.3.1 Upper surface

The distribution of u'/U_∞, v'/U_∞, and $-\overline{u'v'}/U_\infty^2$ as predicted by the different models at locations $x/c = 0.6$, 0.8, and 0.98 are shown in Figs 10 to 12, respectively. Corresponding values obtained from experiments [**24**] are also shown in the same figures. These ratios provide useful information about turbulent boundary-layer structure. u'/U_∞, v'/U_∞, and $-\overline{u'v'}/U_\infty^2$ generally have peak values very close to the surface and gradually fall to small values as the free stream is approached. This aspect is predicted well by all the turbulence models as shown in these figures.

Experimental results show that the maximum value of u'/U_∞ is 0.16 at $x/c = 0.6$. All the models underpredict this value, with the RSM being the closest ($\sim$0.11) to that of the experimental value. From $x/c = 0.6$ to 0.98, two competing phenomena are likely to occur. Concave curvature is expected to increase the turbulence intensity but it is also known that the downstream of reattachment turbulent intensity should reduce. Between $x/c = 0.6$ and 0.98, $|\delta/R|$ varies between 0.0015 and 0.12, and it is expected

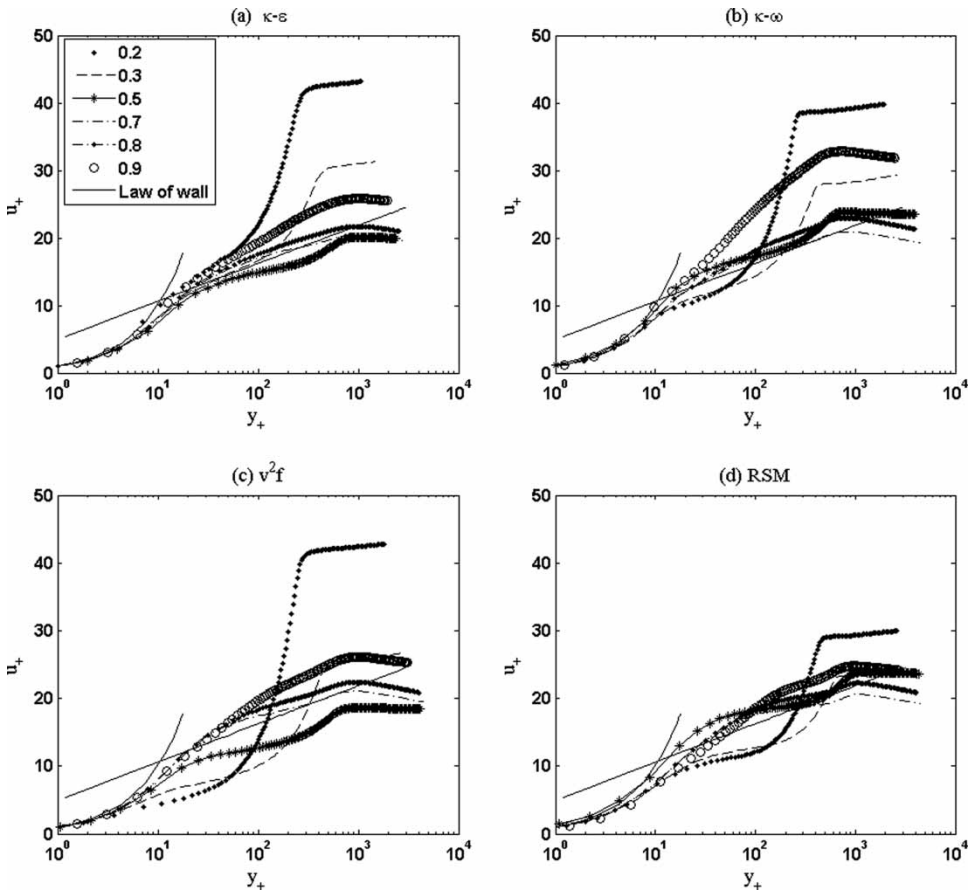

Fig. 9 Semi-logarithmic plot of velocity profile at different stations on the lower surface. k–ε: k–ε realizable; k–ω: k–ω SST; v^2f: $\overline{v'^2}$–f; RSM: Reynolds stress model

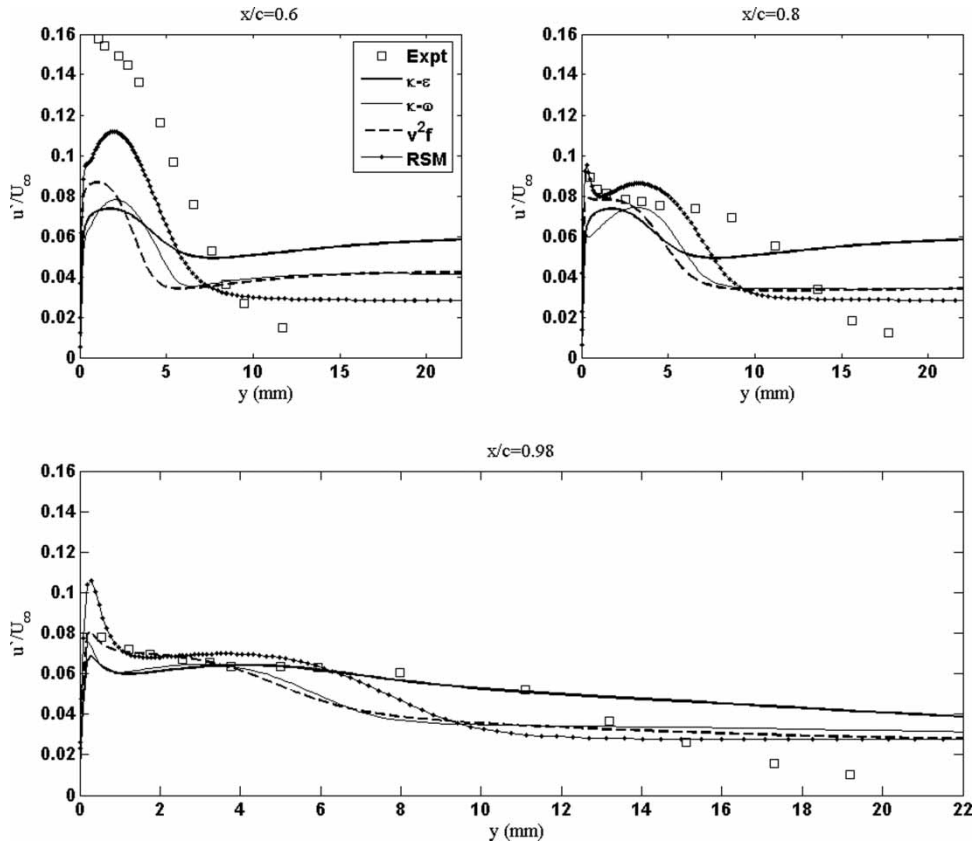

Fig. 10 Variation of u' across the boundary layer on the upper surface of the hydrofoil. Expt: experimental data [**24**]; k–ε: k–ε realizable; k–ω: k–ω SST; v^2f: $\overline{v'^2}$–f; RSM: Reynolds stress model

that the curvature effect will be moderate [**28**]. Experimental as well as numerical results indicate that the curvature effect is less significant when compared with reattachment and turbulent intensity decreases. Of all the models, the RSM seem to capture the qualitative trend best although there is a quantitative difference between the experimental and numerical results.

Figures 11 and 12 show the variations of v'/U_∞ and $-\overline{u'v'}/U_\infty^2$, respectively. Here also, both v'/U_∞ and $-\overline{u'v'}/U_\infty^2$ show a decreasing trend with x/c, thus confirming that the curvature effect is less pronounced. The experimental results indicate that there is a slight shift of the location of the maximum away from the wall, and all the models indicate this fact. For u'/U_∞ and v'/U_∞, the model predictions reach the free stream turbulence level at the end of the boundary layer.

3.3.2 *Lower surface*

Turbulence quantities for different models are compared with the experimental results at different locations on lower surface. These are shown in Figs 13 to 15, respectively.

At $x/c = 0.05$, there is flow separation and the maxima of u'/U_∞, v'/U_∞, and $-\overline{u'v'}/U_\infty^2$ (shown in Figs 13 to 15, respectively) are shifted away from the wall. This was also observed by Simpson *et al.* [**29**] and Shiloh *et al.* [**30**]. Between $x/c = 0.3$ and $x/c = 0.5$, the boundary layer is influenced by the concave curvature, favourable pressure gradient, and there can also be an effect of flow reattachment. Although concave curvature tends to promote turbulence, regions downstream of a reattachment point will tend to have less turbulence intensity. From the experimental and numerical results, it is seen that the maximum values of u'/U_∞, v'/U_∞, and $-\overline{u'v'}/U_\infty^2$ decrease slightly. Thus, the curvature seems to be slightly less effective compared with flow reattachment and this is expected because the maximum value of $|\delta/R|$ in this region is 0.002, and the curvature effect can be considered as mild [**28**]. Experimental u'/U_∞ data show two locations of peak – one near the wall and another away from the wall. The RSM captures this trend better than the other models.

For locations $x/c = 0.6$ and 0.7, the flow has convex curvature and favourable pressure gradient. Experimental data show that u'/U_∞ has its peak near the wall

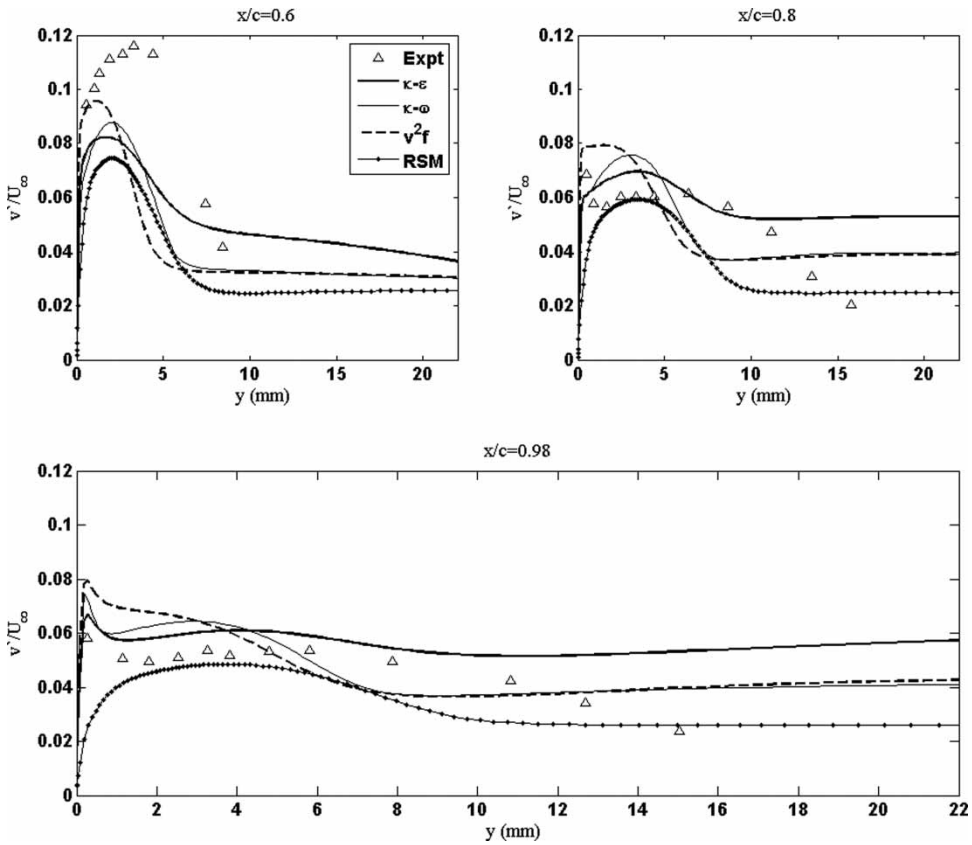

Fig. 11 Variation of v' across the boundary layer on the upper surface of the hydrofoil. Expt: experimental data [**24**]; k–ε: k–ε realizable; k–ω: k–ω SST; v^2f: $\overline{v'^2}$–f, RSM: Reynolds stress model

and remains constant before dropping to free stream value. All the models show a peak near the axis but none of these models could capture the trend well. Experimental v'/U_∞ and $-\overline{u'v'}/U_\infty^2$ data show a peak away from the wall and this feature has been picked only by the RSM. Other models show a peak near the wall.

Points $x/c = 0.8$ and 0.9 are in the region of adverse pressure gradient and convex curvature. Experimental data of u'/U_∞, v'/U_∞, and $-\overline{u'v'}/U_\infty^2$ show one sharp peak near the wall. There is also a second, broadened peak away from the wall. None of the models could capture this feature properly. In general, it is seen that the suppression of the turbulence due to convex curvature is captured better by the RSM and as shown in Fig. 14, the EVM tends to overpredict the turbulence level for flow over convex surface.

A discussion of the successes and limitations of the different turbulent models used in the present work is essential to understand the general applicability of these models to flows having combination of successive changes in curvatures and pressure gradients. It is well known that k–ε models are diffusive in boundary layers subjected to adverse pressure gradients and in the presence of the streamline curvatures [**18**]. The defects arise from the limitations of the linear EVM and also because of their tendency to overestimate the turbulent length scale, and hence the viscosity in decelerating near-wall flows. This results in the separation from continuous surfaces to be inhibited and even if it is predicted, the recirculation region tends to be short. Though the SST model is better than the k–ε models near the wall, yet they also cannot account for anisotropy arising particularly near the curved surfaces. The $\overline{v'^2}$–f model, which includes a transport equation for $\overline{v'^2}$ instead of k and an additional wall-related relaxation equation, which relaxes $\overline{v'^2}$ to k away from the wall, leans heavily on closure ideas pertaining to the Reynolds stress transport modelling [**18**]. Hence, this model can predict the mean and turbulent quantities for flow over both the concave and convex curvatures better than the other EVMs employed in the present study.

Thus, it is seen that of all the turbulent models, the RSM is the best in capturing the experimental trends qualitatively; quantitatively, however,

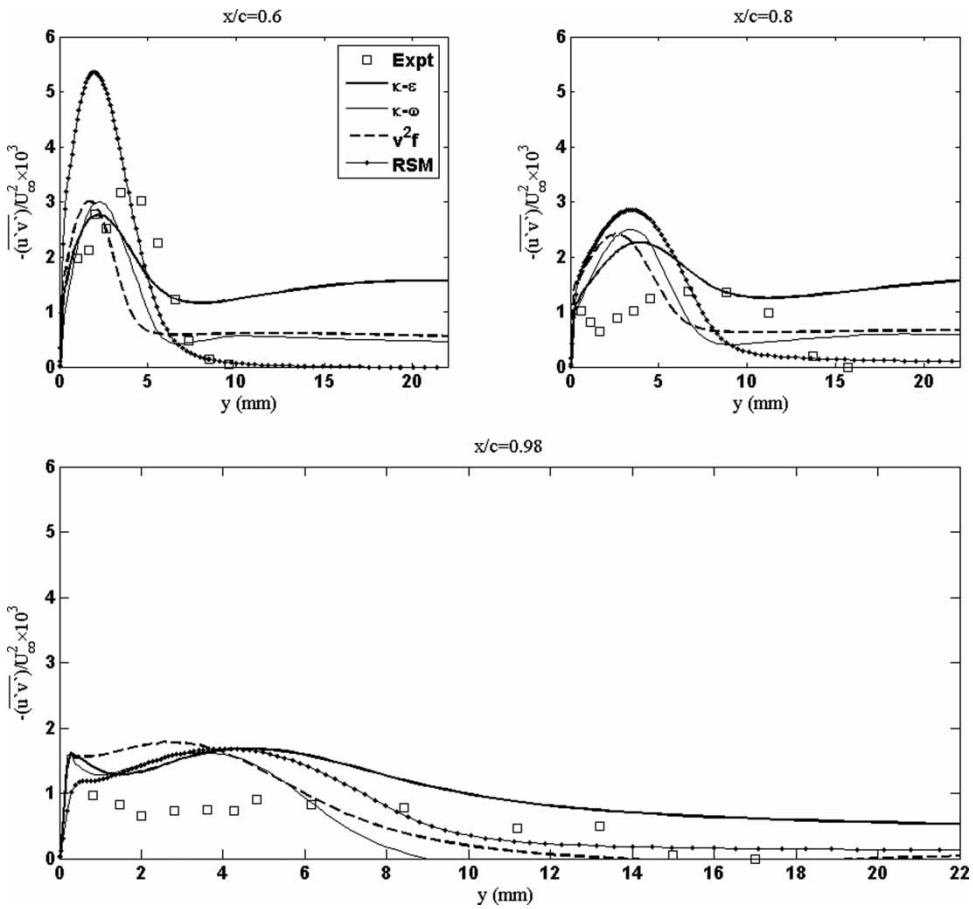

Fig. 12 Variation of $-\overline{u'v'}$ across the boundary layer on the upper surface of the hydrofoil. Expt: experimental data [**24**]; k–ε: k–ε realizable; k–ω: $k-\omega$ SST; v^2f: $\overline{v'^2}$–f; RSM: Reynolds stress model

there exists discrepancies even for this model. Other researchers have also mentioned this fact [**9**, **10**, **15**]. It may be mentioned that the RSM employs k–ε model for estimating ε and so it is felt that the ε equation needs to be modified in order to properly account for the curvature effects. A similar conclusion was drawn by Luo and Lakshminarayana [**10**]. Another problem that arises with the RSM is the modelling of pressure–strain term. In the results presented, linear pressure–strain model was used. Simulation was also carried out with the quadratic pressure–strain model of Speziale *et al.* [**31**] but the results, not reported here, showed no improvement. In fact, the low-Reynolds number modification of the linear pressure–strain relationship along with the wall reflection term presented here predicted results closest to that of the experiments. There is one more plausible reason that might have resulted in the comparisons not so conclusive. There could be a lack of three-dimensional effects in the two-dimensional modelling and simulation. Perhaps, as a result of this, there was a qualitative, and not quantitative, agreement between the numerical results and the experimental trend.

Also, the use of a hot-wire probe for experimental measurement of turbulent fluctuations needs to be subjected to scrutiny. Though the experimental uncertainty in determining the turbulent quantities using a hot-wire probe was not mentioned in the paper by Madhusudan *et al.* [**24**], it is known that determination of these quantities using a hot-wire probe close to the surface poses great difficulty in terms of the exact location of the probe and also produces greater error in their estimation [**28**].

The results presented in this work have in general captured the experimental trend. It is difficult to derive some strict conclusions. But it is clear from the present work that the curvature effects, especially the ones related to flow destablization, lead to the need of enhanced modelling. The main difference, and even an additional aspect, between the already published works on curvature effect and the present work is that unlike the previous geometries, the surface here

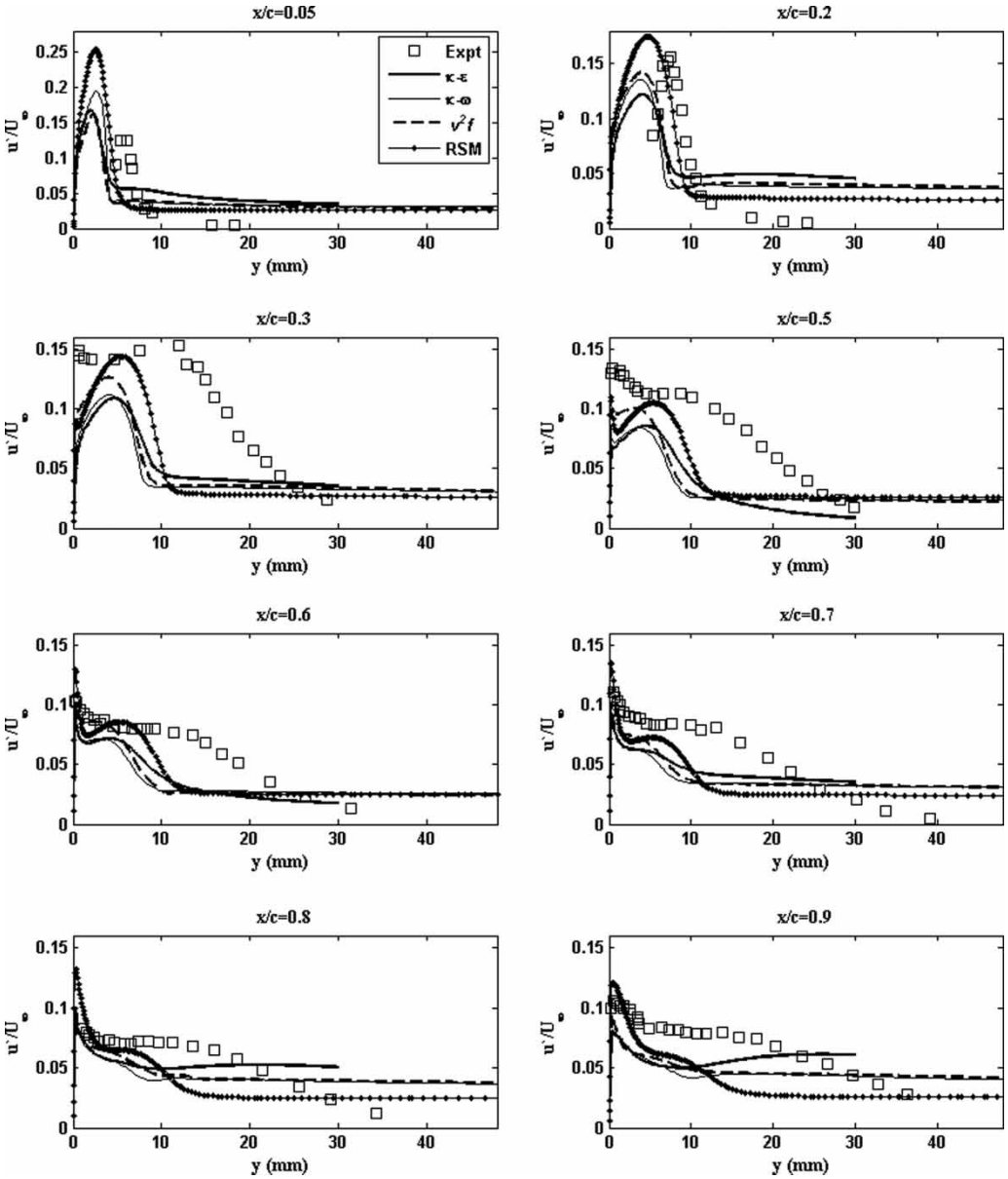

Fig. 13 Variation of u' across the boundary layer on the lower surface of the hydrofoil. Expt: experimental data [**24**]; k–ε: k–ε realizable; k–ω: k–ω SST; v^2f: $\overline{v'^2}$–f; RSM: Reynolds stress model

has consecutive convex and concave curvatures and there is also a simultaneous presence of favourable and adverse pressure gradients. The difference in the order in which the flow approaches the curvatures (like, convex surface followed by concave one on the upper surface and in the reverse order for the lower surface) is also a notable aspect of the present geometry and simulation. Thus, it is felt that this geometry subjects the models to stricter scrutiny of different extra-strain effects. Further, a very close investigation has been performed by reporting all the steps during the modelling of the flow, and comparisons are presented not only for the velocity distributions but also for the Reynolds-stress components.

3.4 Computational cost

Although accuracy in the turbulent flow prediction is of extreme importance in choosing a turbulent model, computational cost is also an important constraint. A brief outline of the computational efforts required in simulating the flow with each of the turbulent models is briefly discussed. In the present work, all simulations were done using the Pentium® 4 CPU 3.40 GHz, 1 GB of RAM hp workstation xw4200. k–ε realizable and k–ω SST models are computationally more efficient: the turbulent flow simulations using these models converge much faster than $\overline{v'^2}$–f and RSM. When compared with the k–ε realizable or k–ω SST model,

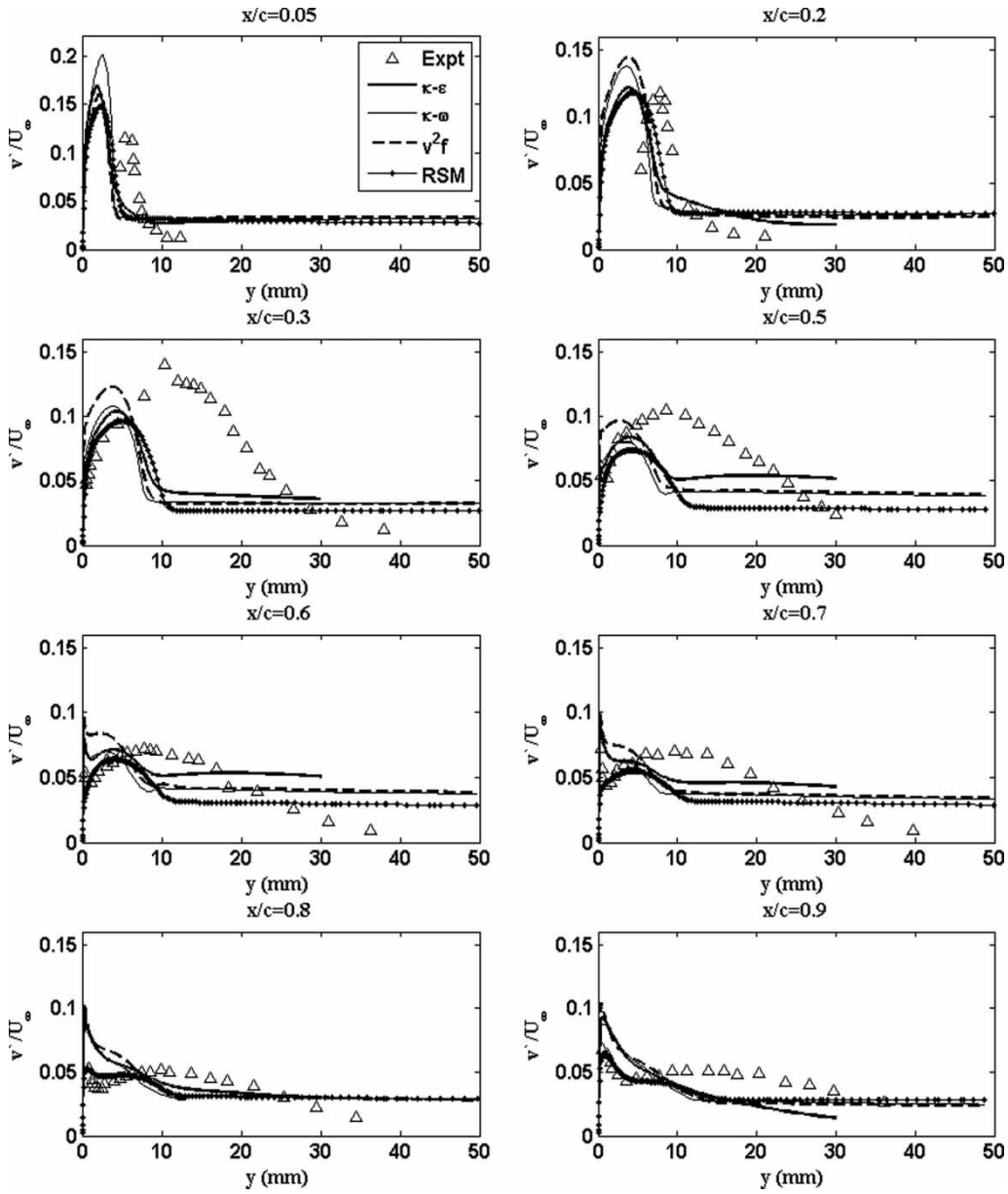

Fig. 14 Variation of v' across the boundary layer on the lower surface of the hydrofoil. Expt: experimental data [**24**]; k–ε: k–ε realizable; k–ω: k–ω SST; v^2f: $\overline{v'^2}$–f; RSM: Reynolds stress model

$\overline{v'^2}$–f, and the RSM, respectively, take about 5 and 22 times more time to reach the defined convergence level of 10^{-5}.

4 CONCLUSION

The turbulent flow over the S-shaped hydrofoil, even at 0° angle of attack, is complicated due to the simultaneous presence of concave and convex surfaces, adverse and favourable pressure gradients, and also flow separation and reattachment. Modelling such a flow poses a formidable challenge. In the present work, four turbulence models, namely, k–ε realizable, k–ω SST, $\overline{v'^2}$–f, and the RSM were examined. Grid independence study was conducted for all the models and, in order to capture the boundary-layer phenomena better, wall y^+ value was maintained <1 in all cases. Comparison of experimental data [**24**] and numerical predictions were made and the suitability of turbulence models was ascertained for both the mean and turbulent quantities. It is seen that in terms of mean quantities like the lift and drag coefficients, the prediction of flow separation and reattachment, $\overline{v'^2}$–f out-performs other models. When it comes to predicting the turbulent quantities, none of the models could match the experimental data quantitatively. Qualitatively, however, RSM matched

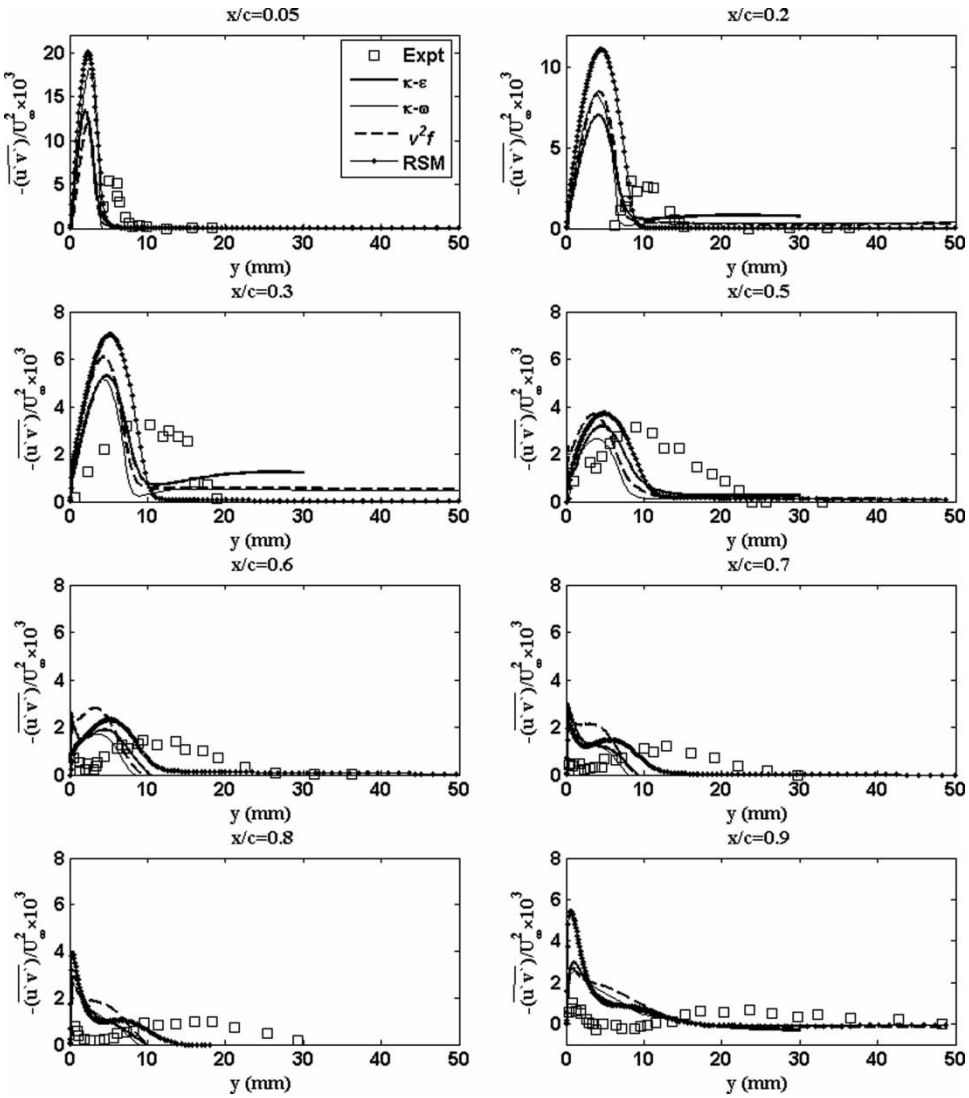

Fig. 15 Variation of $-\overline{u'v'}$ across the boundary layer on the lower surface of the hydrofoil. Expt: experimental data [**24**]; k–ε: k–ε realizable; $k-\omega$: $k-\omega$ SST; v^2f: $\overline{v'^2}-f$; RSM: Reynolds stress model

the experimental data best. The difference between experimental and numerical data could be because of the inability of these models to capture the details shown in the experimental results as has been stated by other researchers in the past. It could also be because of the inherent high uncertainty present in measuring the turbulent quantities using a hot-wire probe and also in exactly determining the location of the probe in regions very close to the surface. In terms of computational cost, k–ε realizable and k–ω SST are the least expensive, and the RSM is more expensive than the other three models.

REFERENCES

1 **Bradshaw, P.** Effects of streamline curvature on turbulent flow. AGARD-AG-169, 1973.

2 **So, R. M. C.** and **Mellor, G. L.** Experiment on convex curvature in turbulent boundary layer. *J. Fluid Mech.*, 1973, **60**, 43–62.

3 **So, R. M. C.** and **Mellor, G. L.** Experiment on turbulent boundary layers on a concave wall. *Aeronaut. Q.*, 1975, **26**, 25–40.

4 **Barlow, R. S.** and **Johnston J. P.** Structure of a turbulent boundary layer on a concave surface. *J. Fluid Mech.*, 1988, **191**, 137–176.

5 **Baskaran, V., Smits, A. J.,** and **Joubert, P. N.** A turbulent flow over a curved hill part 1. growth of an internal boundary layer. *J. Fluid Mech.*, 1987, **182**, 47–83.

6 **Baskaran, V., Smits, A. J.,** and **Joubert, P. N.** A turbulent flow over a curved hill part 2. effect of streamline curvature and streamwise pressure gradient. *J. Fluid Mech.*, 1991, **232**, 377–402.

7 **Gibson, M. M., Jones, W. P.,** and **Younis, B. A.** Calculation of turbulent boundary layers on curved surfaces. *Phys. Fluids*, 1981, **24**(3), 389–395.

8 **Richmond, M. C.** and **Patel, V. C.** Convex and concave surface curvature effects in wall-bounded turbulent flows. *AIAA J.*, 1991, **29**(6), 895–902.

9 **Luo, J.** and **Lakshminarayana, B.** Prediction of strongly curved turbulent duct flows with Reynolds stress model. *AIAA J.*, 1997a, **35**(1), 91–98.

10 **Luo, J.** and **Lakshminarayana, B.** Analysis of streamline curvature effects on wall-bounded turbulent flows. *AIAA J.*, 1997b, **35**(8), 1273–1279.

11 **Davidson, L.** Prediction of the flow around an airfoil using a Reynolds Stress transport model. *Trans. ASME J. Fluids Eng.*, 1995, **117**, 50–57.

12 **Rumsey, C. L.** and **Gatski, T. B**. Turbulence model predictions of extra-strain rate effects in strongly-curved flow. In the 37th Aerospace Sciences Meeting and Exhibit, Reno, NV, 11–14 January 1999, AIAA 99-0157.

13 **Sleiti, A. K.** and **Kapat, J. S.** Comparison between EVM and RSM turbulence models in predicting flow and heat transfer in rib-roughened channels. *J. Turbulence*, 2006, **7**(29), 1–21.

14 **Jing-lei, X. U., Hui-yang, M. A.,** and **Yu-ning, H.** Nonlinear turbulence models for predicting strong curvature effects. *Appl. Math. Mech.-Engl Ed.*, 2008, **29**(1), 31–42.

15 **Yakinthos, K., Vlahostergios, Z.,** and **Goulas, A.** Modeling the flow in a 90° rectangular duct using one Reynolds-stress and two eddy-viscosity models. *Int. J. Heat and Fluid Flow*, 2008, **29**, 35–47.

16 **Balabaskaran, V., Lakshmana Gowda, B. H.,** and **Venkatasubramanian, N.** Flow visualization studies over S-Blades. *J. Flow Vis. Image Process.*, 1998, **5**, 249–259.

17 **Ramachandran, R. M., Radha Krishna, H. C.,** and **Aswatha Narayana, P. A.** Aerodynamic characteristics of 'S' blade profile. *Irrigation Power,* 1984, **41**(2), 205–212.

18 **Leschziner, M. A.** Modelling turbulent separated flow in the context of aerodynamic applications. *Fluid Dyn. Res.*, 2006, **38**, 174–210.

19 **Wilcox, D.** *Turbulence modeling for CFD*, 1993 (DCW Industries Inc, CA).

20 **Durbin, P. A.** Separated flow computations with the k–ε – v^2 model. *AIAA J.*, 1995, **33**, 659–664.

21 **Iaccarino, G.** Predictions of a turbulent separated flow using commercial CFD codes. *J. Fluids Eng.*, 2001, **123**, 819–828.

22 *Fluent® Reference Manual, version 6.2.16*, 2005 (Fluent Inc., Lebanon, NH, USA).

23 **Menter, F. R.** Two equation eddy viscosity turbulence models for engineering applications. *AIAA J.*, 1994, **32**, 1598–1605.

24 **Madhusudan, R. S., Aswatha Narayana, P. A., Balabaskaran, V.,** and **Tulapukara, E. G.** Boundary layer studies over an S-blade. *Fluid Dyn. Res.*, 1994, **14**(5), 241–258.

25 **Madhusudan, R. S.** *Flow studies of S-blade for fully reversible axial flow pump-turbines*. PhD Thesis, IIT Madras, 1992.

26 **Lueptow, M. R., Leehey, P.,** and **Stellinger, T.** The thick, turbulent boundary layer on a cylinder: mean and fluctuating velocity. *Phys. Fluids,* 1985, **28**, 3495–3505.

27 **Willmarth, W. W., Winkel, R. E., Sharma, L. K.** and **Bogar, T. J.** Axially symmetric turbulent boundary layers on cylinders: mean velocity profiles and wall pressure fluctuations. *J. Fluid Mech.*, 1976, **76**, 35–64.

28 **Patel, V. C.** and **Sotiropoulos, F.** Longitudional curvature effects in turbulent boundary layers. *Prog. Aerosp. Sci.*, 1997, **33**, 1–70.

29 **Simpson, R. L., Chew, Y. T.,** and **Shivaprasad, B. G.** The structure of a separating turbulent boundary layer, part 1, mean flow and Reynolds stresses. *J. Fluid Mech.*, 1981, **113**, 23–51

30 **Shiloh, K., Shivaprasad, B. G.,** and **Simpson, R. L.** The structure of a separating turbulent boundary layer, part 3, transverse velocity measurements. *J. Fluid Mech.,* 1981, **113**, 75–90.

31 **Speziale, C. G., Sarkar, S.,** and **Gatski, T. B.** Modeling the pressure-strain correlation of turbulence: an invariant dynamical systems approach. *J. Fluid Mech.,* 1991, **227**, 245–272.

APPENDIX

Notation

c	profile chord
C_{D}	lift coefficient
C_{f}	skin-friction coefficient
C_{L}	drag co-efficient
C_{p}	surface pressure co-efficient $= (P_s - P_{s1})/(P_{t1} - P_{s1})$
k	turbulent kinetic energy
p	pressure
P_{s1}	free stream static pressure
P_{t1}	frees stream total pressure
P_{s}	static pressure
R	radius of curvature
u^*	friction velocity $= (\tau_w/\rho)^{1/2}$
u^+	U/U^*
u', v'	RMS value of turbulent fluctuations along x- and y- directions
$-\overline{u'v'}$	RMS value of Reynolds shear stress
u_i	mean velocity components
U	mean velocity in stream wise direction
U_{e}	external velocity outside the boundary layer
U_∞	free stream velocity
x	distance measured along the chord from leading edge
y_+	$yU^*\rho/\mu =$ viscous distance
y	distance normal to the profile surface
δ	boundary-layer thickness
ε	turbulent dissipation
μ	dynamic viscosity
μ_{t}	eddy viscosity
ν	kinematic viscosity
ν_{t}	kinematic eddy viscosity
ρ	density
τ_{w}	wall shear stress
ω	specific dissipation rate